nature materials

ARTICLES

PUBLISHED ONLINE: 2 MAY 2016 | DOI: 10.1038/NMAT4638

Polymer nanofilms with enhanced microporosity by interfacial polymerization

Maria F. Jimenez-Solomon[1†], Qilei Song[1†], Kim E. Jelfs[2], Marta Munoz-Ibanez[1] and Andrew G. Livingston[1*]

Highly permeable and selective membranes are desirable for energy-efficient gas and liquid separations. Microporous organic polymers have attracted significant attention in this respect owing to their high porosity, permeability and molecular selectivity. However, it remains challenging to fabricate selective polymer membranes with controlled microporosity that are stable in solvents. Here we report a new approach to designing crosslinked, rigid polymer nanofilms with enhanced microporosity by manipulating the molecular structure. Ultrathin polyarylate nanofilms with thickness down to 20 nm are formed *in situ* by interfacial polymerization. Enhanced microporosity and higher interconnectivity of intermolecular network voids, as rationalized by molecular simulations, are achieved by using contorted monomers for the interfacial polymerization. Composite membranes comprising polyarylate nanofilms with enhanced microporosity fabricated *in situ* on crosslinked polyimide ultrafiltration membranes show outstanding separation performance in organic solvents, with up to two orders of magnitude higher solvent permeance than membranes fabricated with nanofilms made from non-contorted planar monomers.

Conventional gas and liquid separation processes such as evaporation and distillation are widely used in the oil and gas, energy, chemical, and pharmaceutical industries, but are energy intensive. An alternative to these processes is membrane separation technology, which typically consumes an order of magnitude less energy. To enable wider deployment of membrane technology, highly permeable membranes are required to process large volumes of gas or solvent using a viable membrane area over a feasible time frame[1,2]. There are two main strategies being followed to this end. One is to design the polymer structure at the molecular level so as to provide greater interconnected microporosity[3–10], whereas a second approach is to reduce the thickness of the separating layer to the nanometre scale[11–16].

Microporous organic materials with well-defined pore structures are excellent candidates for highly permeable and selective membranes[1], such as metal–organic frameworks (MOFs) and porous coordination polymers[17,18], covalent organic frameworks[19,20], and porous organic cages[21–23]. However, the fabrication of these crystalline solids to form defect-free membranes is technically challenging. Recent significant progress includes fabrication of MOFs to form selective membranes by secondary crystal growth[24], assembly of MOF nanosheets[15], interfacial synthesis[25], or mixed matrix membranes[10,26]. In contrast, industrial membranes are dominated by solution processing of polymers and interfacial polymerization, for example in producing polyamide desalination membranes. Notable examples of microporous polymers are polymers of intrinsic microporosity (PIMs)[6,7,27–31]. Owing to the shape and rigidity of the component monomers, the polymer chains have contorted, rigid backbones resulting in inefficient packing, creating interconnected voids of less than 2 nm that behave as micropores. Owing to their solubility in common solvents, linear-type PIMs can be processed into thin films that are highly permeable and selective for gas separations[32,33]. However, it is this solubility in a range of solvents that restricts their applications in organic solvent nanofiltration (OSN)[34,35]. Several efforts to make these PIM thin films solvent resistant have been reported, including thermal oxidative crosslinking[9], chemical crosslinking[28], and blending with thermally reactive polymers[34]; however, these approaches introduce further processing steps.

Efforts to achieve higher separation performance, particularly higher permeance, have also sought to create ever-thinner membranes, such as PIM-1 nanofilms[36], and MOF nanosheets[15]. Unexpectedly, recent work has shown that decreasing the thickness of solution-cast films of PIM-1 below 100 nm resulted in a decrease, rather than an increase, in heptane permeance[36]. This was attributed to structural relaxation of the polymer molecules in the thin films. This effect has also been observed in gas permeation[37], and suggests that linear macromolecules may not be suitable for ultrathin nanofilms. In contrast, for nanofilms comprising crosslinked polymer networks or carbon networks, solvent permeance continues to increase as thickness is reduced. Fabrication of freestanding ultrathin nanofilm membranes using metal hydroxide nanostrands as sacrificial substrates[38,39] was recently extended to the formation of crosslinked polyamide nanofilms by interfacial polymerization followed by dimethylformamide (DMF) activation[11]. The resulting highly permeable ultrathin freestanding polyamide nanofilms offer superior performance to conventional filtration membranes; however, sophisticated nanoscale processing steps are required in their fabrication.

Previous work indicates that introducing rigid moieties into polyamide nanofilms with thickness of 100 nm made by interfacial polymerization enhances nanofilm porosity[40]. Nanofiltration performance was demonstrated for removal of salts from water, but these polyamide membranes had defects, limiting their application to other molecular separations[40].

Here we report a new synthetic approach to designing polymer nanofilm membranes with enhanced microporosity without complex processing. We employed interfacial polymerization with

[1]Department of Chemical Engineering, Imperial College London, London SW7 2AZ, UK. [2]Department of Chemistry, Imperial College London, London SW7 2AZ, UK. [†]These authors contributed equally to this work. *e-mail: a.livingston@imperial.ac.uk

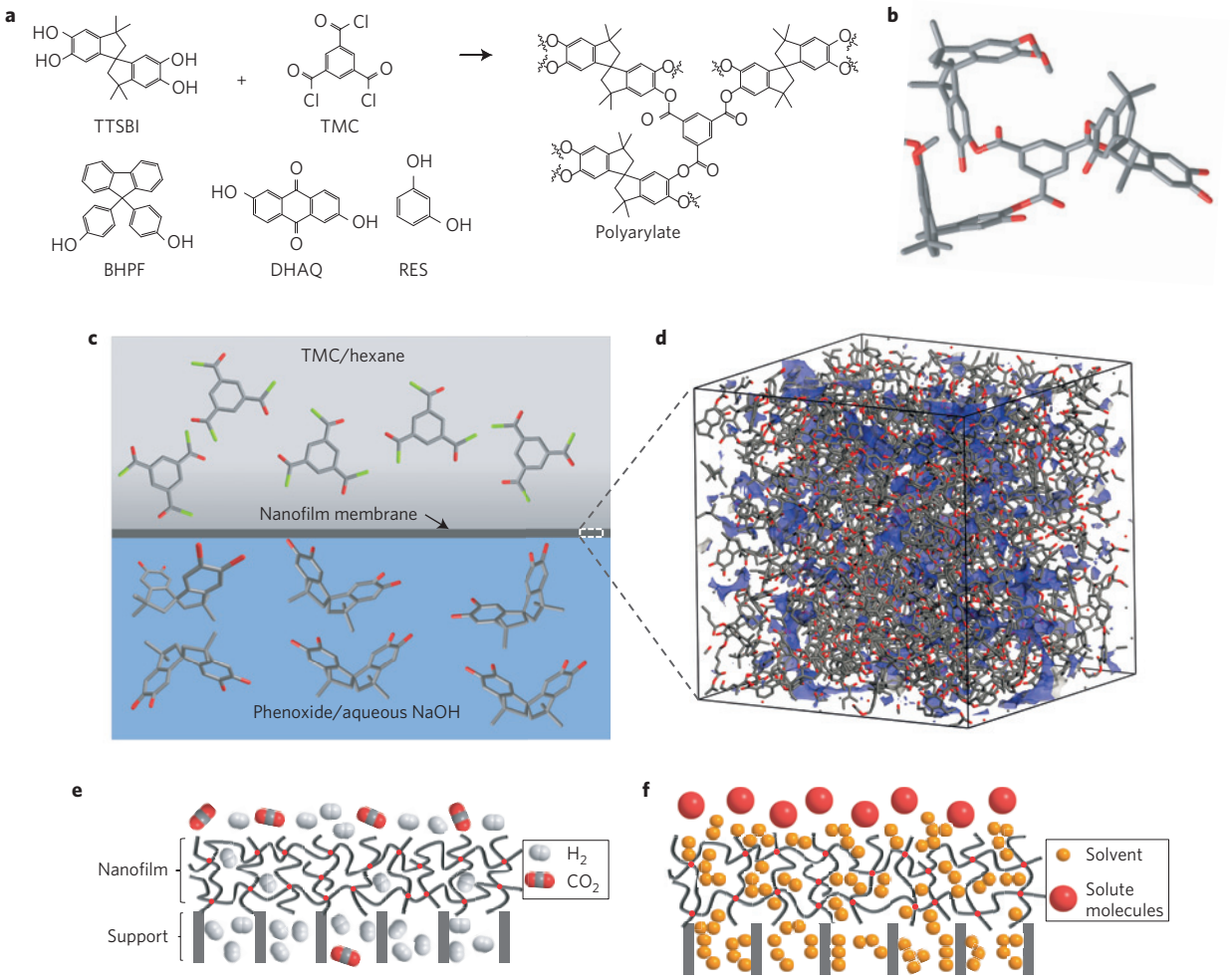

Figure 1 | Interfacial synthesis of polyarylate nanofilms. a, Synthesis of aromatic polyester (polyarylate) nanofilms through interfacial polymerization. The aromatic phenol is dissolved in a dilute sodium hydroxide solution and reacts with trimesoyl chloride (TMC) dissolved in hexane at the hexane/aqueous interface. Four different phenol monomers were used: spiro-structured 5,5′,6,6′-tetrahydroxy-3,3,3′,3′-tetramethylspirobisindane (TTSBI), cardo-structured 9,9-bis(4-hydroxyphenyl)fluorene (BHPF), and planar-structured 2,6-dihydroxyanthraquinone (DHAQ), and 1,3-benzenediol (RES). The cardo- and spiro-structured monomers are contorted, rigid monomers; DHAQ and RES are monomers with planar structures. **b**, Molecular model of a segment of polyarylate network containing spiro-contorted monomers from TTSBI. **c**, Visualization of the interfacial polymerization between TMC in hexane and the phenoxide of TTSBI in aqueous NaOH solution. **d**, Three-dimensional view of an amorphous cell containing a spiro-contorted PAR-TTSBI polyarylate network. Blue colour: accessible surface at probe radius of 1 Å. Cell size: 46 Å × 46 Å × 46 Å. **e**, Schematic diagram of a polyarylate nanofilm composite membrane used as a selective membrane for gas separations. **f**, Schematic diagram of a polyarylate nanofilm composite membrane used as a solvent-stable selective membrane for OSN, allowing rapid solvent transport while rejecting large solute molecules.

contorted and non-contorted monomers to synthesize defect-free, highly crosslinked polyarylate nanofilms down to 20 nm in thickness directly on ultrafiltration supports. The nanofilms fabricated with contorted monomers exhibit higher microporosity and interconnectivity than those made from non-contorted monomers. This results in up to two orders of magnitude higher permeance for organic solvents, and higher adsorption for gases. We suggest that following interfacial polymerization, the contorted monomers are held in non-coplanar orientations by the network structure, enhancing interconnectivity of intermolecular voids. This hypothesis is supported by our experimental results and molecular simulations. This work demonstrates that interfacial synthesis using contorted monomers provides nanofilms with a wide range of solvent resistance, tunable structural diversity and enhanced microporosity defined by the geometry of monomers.

Polymer nanofilm synthesis by interfacial polymerization

We selected the interfacial polymerization technique because it gives highly crosslinked polymer nanofilms *in situ*, ensuring stability in organic solvents. This simple, reproducible, and easily controllable technique has been used for synthesis of polyamide membranes for applications in reverse osmosis desalination and organic solvent nanofiltration[11,41], MOF capsules[42] and gas separation membranes[25]. Here, polyarylate (PAR) (aromatic polyester) nanofilms were formed by reacting a phenol with trimesoyl chloride (TMC) at the interface between two immiscible solutions (Fig. 1a,c and Supplementary Fig. 1). We used contorted phenols including spiro-structured 5,5′,6,6′-tetrahydroxy-3,3,3′,3′-tetramethylspirobisindane (TTSBI) and cardo-structured 9,9-bis(4-hydroxyphenyl)fluorene (BHPF) to form polyarylates with enhanced microporosity, and selected dihydroxyanthraquinone (DHAQ), and 1,3-benzenediol (RES) with planar structures as non-contorted controls (Fig. 1a and Supplementary Figs 2 and 3). The spiro-centre within TTSBI has an angle of 90°, so when it reacts with TMC the TTSBI units are held in non-coplanar orientation by the polymer network (Fig. 1b), enhancing interconnectivity of network voids. The spiro-centre prohibits the efficient packing of polymer segments in the

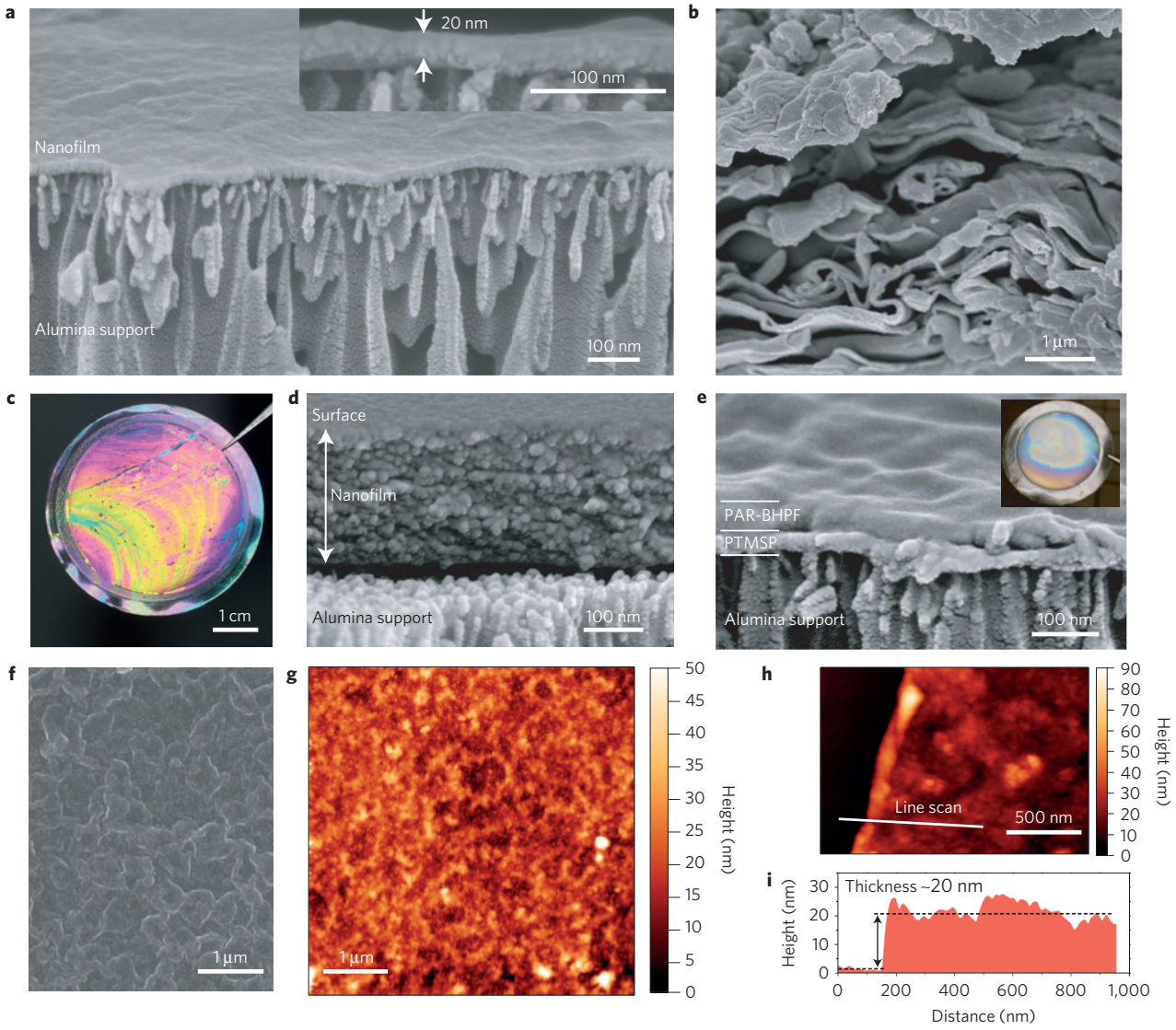

Figure 2 | Polyarylate nanofilms. a, Cross-sectional SEM image of an ultrathin freestanding polyarylate (PAR-TTSBI) nanofilm supported on porous alumina. The nanofilm was prepared by interfacial polymerization of TTSBI (1 wt%) in NaOH/water with TMC (0.1 wt%) in hexane. Right inset: enlargement of the cross-section without tilting. **b**, SEM image of interfacially polymerized cardo-contorted polyarylate (PAR-BHPF) solids with nanofilm morphology, prepared by rigorous mixing of a solution of TMC in hexane added to a solution of BHPF in NaOH/water. **c**, A photograph of a thicker freestanding defect-free PAR-BHPF nanofilm supported on a porous alumina support (diameter of 47 mm) held by tweezers. **d**, Cross-sectional SEM image of the PAR-BHPF nanofilm supported on a porous alumina support. **e**, Cross-sectional SEM image of the cardo-structured PAR-BHPF nanofilm supported on PTMSP/alumina. PAR nanofilms were prepared by sequential spin-coating of a solution of TMC in hexane and a solution of phenol in NaOH/water on PTMSP/alumina. Inset shows a photo of the nanofilm composite membrane (tested in gas permeation). **f**, SEM image of the surface of a PAR-TTSBI nanofilm interfacially polymerized on a crosslinked P84 polyimide membrane support. **g**, AFM image probed on the sample shown in **f**. **h**,**i**, AFM image (**h**) and corresponding height profile (**i**) of a section of a PAR-TTSBI nanofilm on top of a silicon wafer. A scratch was made to expose the wafer surface and allow measurement of the height from the silicon wafer surface to the upper nanofilm surface.

networks, leading to relatively higher free volume. Figure 1d shows a three-dimensional view of a modelled amorphous cell containing a porous PAR-TTSBI network. To exploit their rigidity, solvent stability and enhanced porosity, we synthesized PAR nanofilms directly on porous supports and used them as selective membranes for gas separations and organic solvent nanofiltration (Fig. 1e,f).

Polyarylate nanofilms with thickness down to 20 nm can be formed through interfacial polymerization (Fig. 2a), and were transferred onto anodized alumina supports, allowing clear imaging with scanning electron microscopy (SEM; Supplementary Fig. 4). The nanofilm thickness can be tuned by varying the concentration of monomers (Supplementary Figs 4 and 5). To study the morphology and bulk properties of each polyarylate, we synthesized PAR powders through interfacial polymerization in a two-phase mixed reactor with rigorous stirring (PAR-IP; Supplementary Fig. 2), and in monophasic liquid reactions (PAR-MP) (Supplementary Fig. 3). Polymer solids made interfacially show film-like morphologies (Fig. 2b and Supplementary Fig. 6), whereas powders from monophasic reactions show agglomerated particles (Supplementary Fig. 7). Their chemical structure as aromatic polyesters was validated using infrared spectroscopy (Supplementary Fig. 8). Wide-angle X-ray scattering patterns confirm that these polymers are essentially amorphous except for PAR-DHAQ made by interfacial polymerization, which shows some crystalline peaks possibly due to crystallization of monomers (Supplementary Fig. 9). The lattice spacings in wide-angle X-ray scattering for PAR polymers corre-

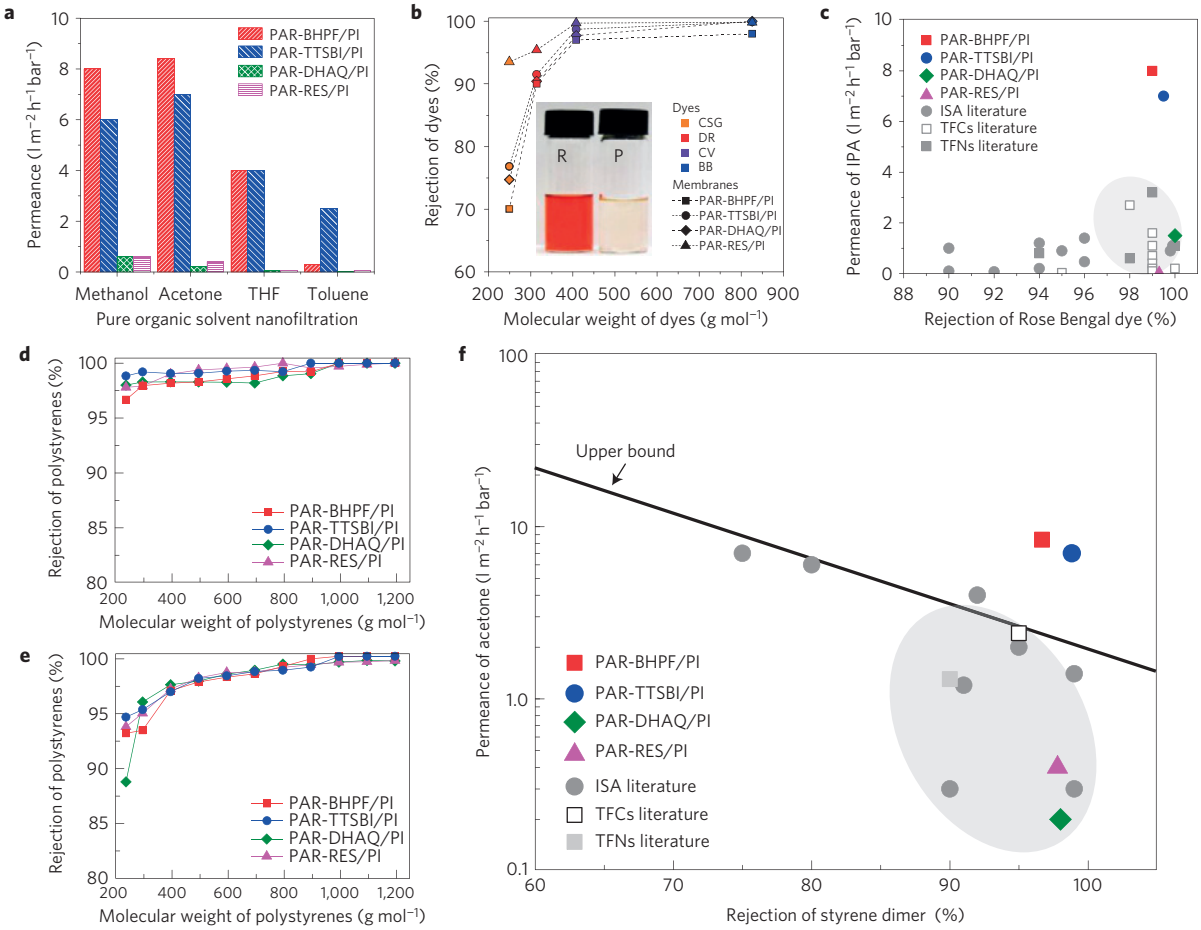

Figure 3 | Organic solvent nanofiltration. a, Pure solvent permeances for methanol, acetone, tetrahydrofuran (THF) and toluene through polyarylate (PAR) nanofilm composite membranes prepared on crosslinked polyimide (PI) supports. Nanofiltration was conducted in a crossflow filtration system at 30 °C under 30 bar. **b**, Rejection versus molecular weight of dyes: brilliant blue (BB, 826 g mol^{-1}); crystal violet (CV, 408 g mol^{-1}); disperse red (DR, 314 g mol^{-1}); and chrysoidine G (CSG, 249 g mol^{-1}) in methanol. Inset photo shows the retentate (R, left) and permeate (P, right) samples for PAR-RES/PI. Nanofiltration was conducted separately for each dye in a crossflow filtration system at 30 °C under 30 bar. **c**, Isopropanol (IPA) permeance versus the rejection of Rose Bengal (1,017 g mol^{-1}) for polyarylate/PI nanofilm composite membranes versus typical integrally skinned asymmetric (ISA), thin-film composite (TFC), and thin-film nanocomposite (TFN) membranes reported in the literature[2]. Nanofiltration was conducted in a dead-end stirred cell (500 r.p.m.) at 30 °C under 30 bar. **d**,**e**, Rejection versus the molecular weight of polystyrene oligomers for polyarylate/PI nanofilm composite membranes. Nanofiltration of a feed solution comprising polystyrene oligomers dissolved in acetone (**d**) or THF (**e**), respectively was conducted in a crossflow filtration system under 30 bar at 30 °C. **f**, The permeance of acetone versus rejection of α-methyl styrene dimer (236 g mol^{-1}) for polyarylate/PI nanofilm composite membranes. Typical nanofiltration data of ISA membranes, TFC membranes and TFN membranes reported in the literature are included[2]. Based on the reported literature value, the upper-bound line is manually added to show a trade-off between permeance of solvent and rejection of solute molecules.

spond well with the level of microporosity observed in gas sorption and modelling. Thermal analysis of all powders revealed high-temperature stability, with decomposition temperature above 400 °C under nitrogen atmosphere (Supplementary Fig. 10).

Polyarylate nanofilms formed at the interface of organic/aqueous monomer solutions can be captured and supported on a porous support, for example, anodized alumina membrane discs (Fig. 2a,c,d). An alternative (and more practical for scale-up) approach is to fabricate nanofilms directly on polymer support membranes. Nanofilm composite membranes for gas separations were prepared *in situ* on poly(trimethylsilyl)propyne (PTMSP)/alumina supports through interfacial polymerization of monomers sequentially spin-coated on the substrates. A thin film of PTMSP (50 nm) was coated as an intermediate layer to assist with PAR film formation. Cross-sectional SEM images show similar nanofilm thicknesses (∼50 nm) for all PAR nanofilms made on PTMSP/alumina supports (PAR/PTMSP; Fig. 2e and Supplementary Fig. 11), enabling comparison of their gas permeances. Nanofilm composite membranes for OSN were prepared directly on crosslinked P84 polyimide (PI) ultrafiltration supports and their surface morphologies characterized using SEM and atomic force microscopy (AFM; Supplementary Fig. 12). PAR-TTSBI made on crosslinked PI support (PAR-TTSBI/PI) shows a smooth surface (Fig. 2f,g). Lack of contrast between PI supports and PAR nanofilms did not allow determination of the nanofilm thickness using SEM. Instead, we transferred a PAR-TTSBI/non-crosslinked PI nanofilm in a flipped configuration onto a silicon wafer and dissolved the PI support[11,43]. We then scratched the nanofilm to reveal the wafer surface and measured the height from the silicon wafer to the nanofilm surface using AFM, giving a thickness of ∼20 nm (Fig. 2h,i). The thickness of these supported nanofilms is similar to that of freestanding PAR-TTSBI nanofilms formed at the organic/aqueous interface using the same monomer concentrations (Fig. 2a). The Young's modulus of a 50-nm-thick PAR-TTSBI nanofilm was estimated as 4.8 GPa through wrinkling-based measurements under compressive stress induced by an elastomer substrate (Supplementary Fig. 13 and Supplementary Table 1). This is higher than values reported for PIM-1 films[9], or

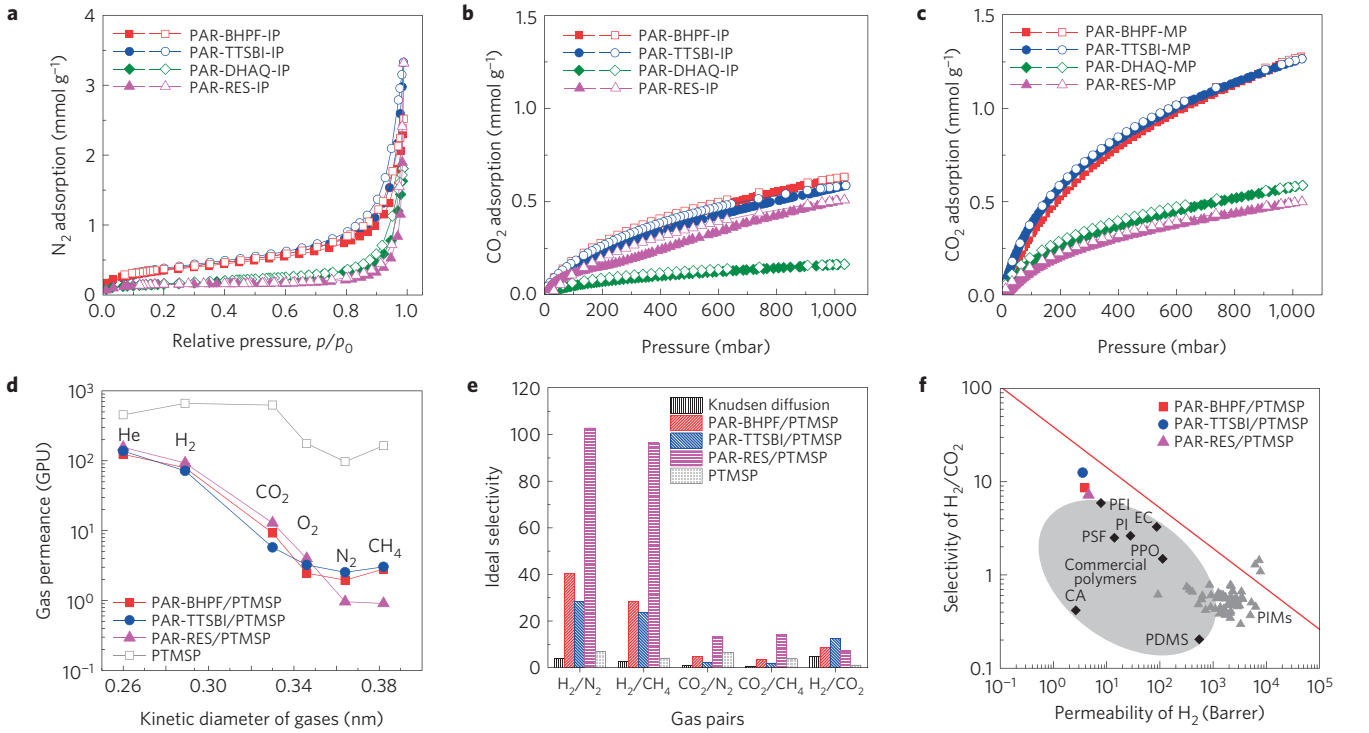

Figure 4 | Gas sorption and transport properties. a,**b**, N_2 sorption at 77 K (**a**) and CO_2 sorption at 273 K (**b**) for polyarylate (PAR) networks prepared through interfacial polymerization (IP). **c**, CO_2 sorption at 273 K for PAR networks synthesized through monophasic (MP) reaction. Symbols in **a**–**c**: filled, adsorption; open, desorption. **d**, Gas permeance as a function of kinetic diameter of gas molecules through PAR nanofilm composite membranes supported on PTMSP thin films (50 nm) coated on alumina. Gas permeation unit (GPU): 1 GPU = 10^{-6} cm^3 (STP) s^{-1} cm^{-2} cm Hg^{-1}. **e**, Ideal gas selectivity for typical gas pairs. **f**, Upper-bound plot of H_2/CO_2 selectivity versus permeability of H_2 for PAR nanofilms. Permeability data are calculated on the basis of the thickness of the PAR layer. The upper bound of polymeric membranes is plotted (red line)[45]. Commercial polymers are included for comparison: cellulose acetate (CA); ethyl cellulose (EC); Matrimid 5218 polyimide (PI); polyetherimide (PEI); polyphenyleneoxide (PPO); polysulfone (PSF); poly(dimethylsiloxane) (PDMS). Typical high-free-volume PIM polymers (dark grey triangles) are included[46].

smooth polyamides prepared through interfacial polymerization[11], confirming the robustness of the PAR nanofilms.

Enhanced microporosity for rapid and selective transport

The effects of using contorted monomers in PAR nanofilms on the selectivity and solvent permeance of PAR/PI nanofilm composite membranes are presented in Fig. 3a. For all PAR/PI membranes, we found that methanol and acetone, with lower molar volume and higher solubility parameter due to dipole force (δ_p) (Supplementary Table 2), gave higher permeance (Fig. 3a and Supplementary Table 3), followed by tetrahydrofuran (THF), and finally toluene. This suggests that molar volume and solvent polarity control solvent permeance. Crosslinked PI support is known to undergo physical ageing and compaction with applied pressure[11], causing a decrease in permeance for PAR/PI membranes of about 45% over the first 5 h of nanofiltration until steady state is reached (Supplementary Fig. 14). All reported permeance data in this work have been collected after this steady state was established. We also tested the OSN performance of a freestanding PAR-BHPF nanofilm (200 nm thick) on an anodized alumina disc (Supplementary Fig. 14); no decreases in permeance over time were observed for any of the solvents, confirming that the decrease in permeance is attributable to the PI support. We were unable to prepare defect-free 20-nm-thick freestanding nanofilms on alumina with areas large enough for filtration tests, and so could not measure permeance of thinner films in this way. The PAR/PI membranes made from contorted monomers (TTSBI, BHPF) show much higher permeances for all solvents compared with PAR/PI membranes made from non-contorted, planar monomers (DHAQ, RES). In particular, the permeance of THF in PAR-TTSBI and PAR-BHPF is as high as 4.0 l m^{-2} h^{-1} bar^{-1}, which is 100 times higher than PAR-RES (0.04 l m^{-2} h^{-1} bar^{-1}). The rejection of dyes is higher for the PAR-RES/PI membrane, as shown by the photographs of dye solutions (inset photograph in Fig. 3b and Supplementary Fig. 15), and effectively the same for the PAR/PI membranes made with other monomers (Fig. 3b and Supplementary Tables 4 and 5). Rejections of styrene oligomers of different molecular weights in different solvents (Fig. 3d,e and Supplementary Fig. 16) are the same for all PAR/PI membranes. The marked increase in permeance for the nanofilm membranes with enhanced microporosity is attributed to contorted species within these PAR nanofilms, confirming our hypothesis. Figure 3c,f shows Rose Bengal rejection versus isopropanol permeance, and α-methyl styrene dimer rejection versus acetone permeance, respectively for our PAR/PI membranes and polymeric OSN membranes reported in the literature[2]. Compared with these previously reported membranes[2], the PAR nanofilm composite membranes with enhanced microporosity from this work show outstanding solvent permeance at the same selectivity.

A comparison between the OSN performance of polyarylate nanofilms with enhanced microporosity and previously reported sub-10-nm polyamide nanofilms[11] is provided in Supplementary Table 6. For nanofilm composite membranes using crosslinked PI supports, the polyarylate nanofilms offer comparable or better permeance than the polyamide nanofilms formed using nanostrands. The nanofilms mounted on alumina supports are harder to compare directly as their thicknesses differ widely. We note that among the polyamide nanofilms it is uniquely the *m*-phenylenediamine-based nanofilms that exhibit increased effective area through crumpling, and that respond favourably to DMF activation. *m*-phenylenediamine and TMC are conventional

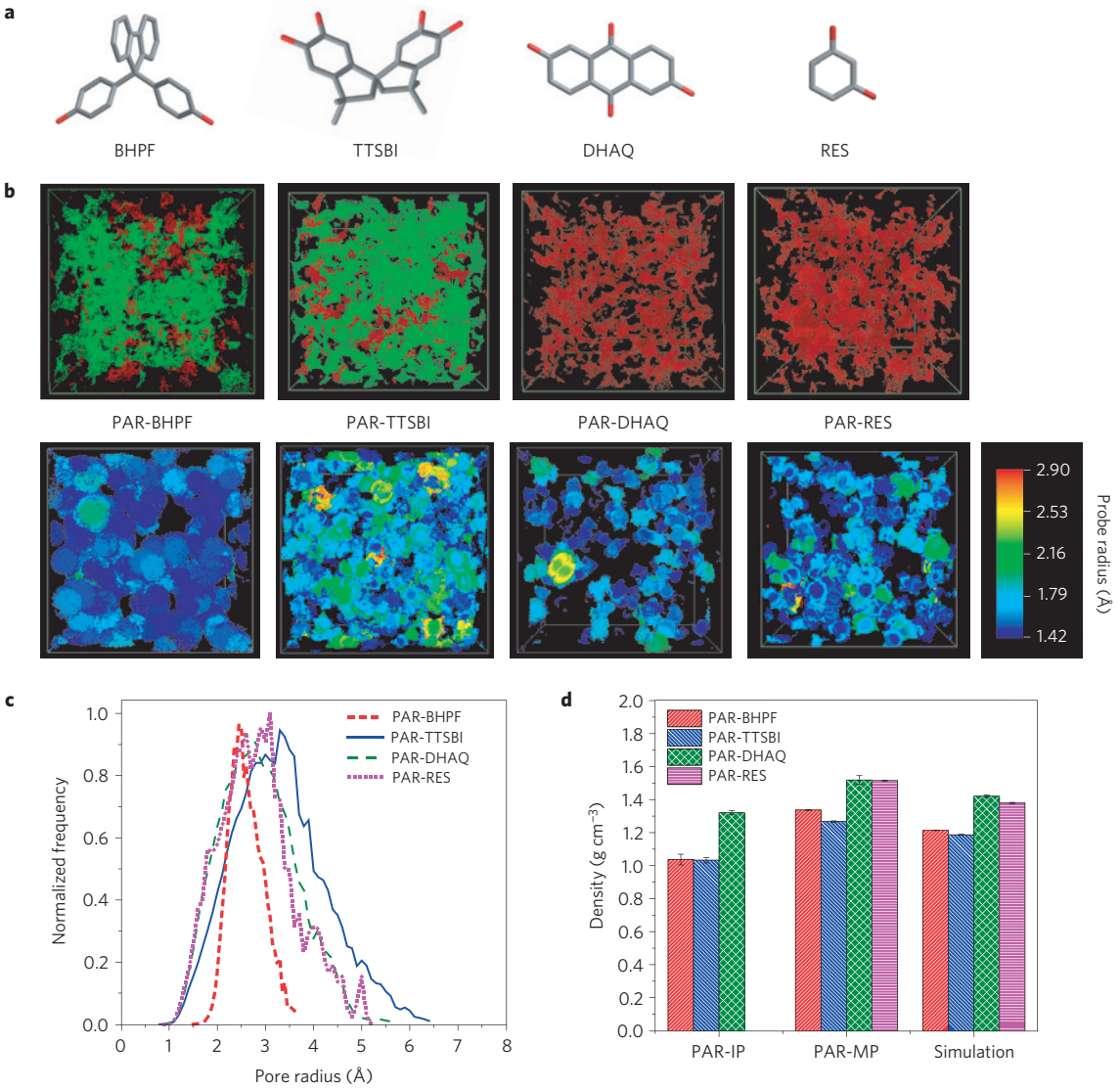

Figure 5 | Structural analysis of amorphous polymer models. a, Three-dimensional molecular model of phenol monomers. **b**, Top row shows the interconnected (green) and disconnected (red) voids with respect to a probe of 0.85 Å radius—this is the largest size probe that can diffuse across any of the rigid models. These images highlight the difference between PAR-BHPF and PAR-TTSBI versus PAR-DHAQ and PAR-RES. Bottom row shows voids coloured with respect to the pore radius. Only voids that are larger than a radius of 1.42 Å (the kinetic radius of H_2) are shown. **c**, Simulated pore size distributions averaged over five models for each of the polyarylate systems. **d**, Experimentally measured density of polyarylates prepared through interfacial polymerization (PAR-IP) or through monophasic (PAR-MP) reaction versus simulated density values.

monomers for desalination membranes, and the exceptional performance of the nanofilms derives from the complex nanoscale fabrication. However, there are significant challenges around the scale-up of both nanostrand fabrication and DMF activation. In contrast, our polyarylate nanofilms are produced *in situ* on ultrafiltration support membranes using regular interfacial polymerization techniques, and their high permeance is due to the non-conventional contorted monomers employed. This supports designing the molecular architecture of nanofilms, using a wide range of chemistries, as an attractive alternative to the use of complex processing steps, to produce high-permeance membranes.

Gas sorption and molecular modelling

N_2 adsorption isotherms at 77 K show low amounts of adsorption (Fig. 4a), with Brunauer–Emmett–Teller surface areas lower than 40 $m^2 g^{-1}$ even for PAR polymers made from contorted monomers (Supplementary Table 7). This suggests restricted access of N_2 molecules within the narrow micropores in these rigid polymer networks. Low nitrogen uptake has been previously reported for other microporous polymers[44], so further investigation used adsorption of CO_2 at 273 K. CO_2 has a smaller kinetic diameter than N_2 (3.3 Å for CO_2 and 3.64 Å for N_2), so it can access micropores that are inaccessible to N_2. PAR-BHPF and PAR-TTBI have higher Brunauer–Emmett–Teller areas (Supplementary Table 7) and higher CO_2 sorption (Fig. 4b,c) than PAR-DHAQ and PAR-RES, with a characteristically steep uptake at low relative pressure particularly for PAR-MP powders, corroborating the microporous nature of PAR powders made from contorted monomers. PAR-MP powders show higher CO_2 sorption (Fig. 4c) than PAR-IP powders (Fig. 4b), possibly due to entrapment of starting materials and solvents in between films formed during interfacial polymerization with rigorous stirring. The CO_2 adsorption isotherms were analysed with the Langmuir model, giving much higher specific surface area for polyarylate nanofilms made from contorted monomers

($150–160\ m^2\ g^{-1}$) through monophasic reaction, compared with polyarylates made from non-contorted monomers ($61\ m^2\ g^{-1}$).

We prepared defect-free PAR nanofilms supported on PTMSP (PAR/PTMSP) and studied single-gas permeations at 295 K with gas molecules of different kinetic diameters, including He (2.60 Å), H_2 (2.89 Å), CO_2 (3.3 Å), O_2 (3.46 Å), N_2 (3.64 Å) and CH_4 (3.8 Å). The intermediate thin layer of PTMSP ages (Supplementary Fig. 17). However, it still gives sufficiently high gas permeance that allows the measurement of intrinsic gas transport properties of the relatively dense PAR nanofilms. As shown in Fig. 4d, gas permeance for PAR/PTMSP membranes decreases as He > H_2 > CO_2 > O_2 > $N_2 \approx CH_4$, suggesting a molecular sieving separation, consistent with the selective permeation of solvents. The PAR-RES nanofilms show much lower permeances for large gas molecules (for example, N_2 and CH_4), resulting in much higher selectivities of small gas molecules over larger ones (H_2/N_2 and H_2/CH_4 up to 100), as shown in Fig. 4e. The PTMSP thin film supported on alumina shows no selectivity for H_2/CO_2, confirming that H_2/CO_2 selectivity for PAR/PTMSP membranes is due to the molecular sieving effect of the PAR nanofilms. Figure 4f shows a plot of H_2/CO_2 selectivity versus the permeability of H_2 for the PAR nanofilms, calculated on the basis of the thickness of the PAR layer, along with the upper-bound limit of polymer membranes[45], including the fast-growing family of PIM polymers[46]. PAR-TTSBI and PAR-BHPF membranes show higher selectivity compared with polymer membranes with similar H_2 permeability, placing them close to the upper bound.

To investigate the pore structures of PAR networks, we performed molecular simulations to generate realistic structural models and analyse their properties. The amorphous polymer models were generated using Polymatic[47], a simulated polymerization algorithm. Details of the molecular simulation are given in the Methods (Supplementary Tables 7 and 8). We generated five models for each system to ensure adequate sampling and averaged the properties across them (Supplementary Figs 18 and 19). Figure 5a shows the monomers with different geometry. The top row images in Fig. 5b show interconnected and disconnected voids with respect to a probe with a radius of 0.85 Å. PAR-BHPF and PAR-TTSBI show mostly interconnected voids, confirming our hypothesis that using contorted monomers results in nanofilms with enhanced microporosity and interconnectivity. In contrast, PAR-DHAQ and PAR-RES show isolated voids, confirming their lower porosity. The bottom row images in Fig. 5b show voids coloured with respect to the largest radius probe that can be inserted. In Supplementary Fig. 19, PAR-BHPF and PAR-TTSBI exhibit substantially more pore volume than the corresponding three-dimensional models of PAR nanofilms made from planar monomers. Pore size distributions for each PAR polymer network were derived from these simulations, showing similar values. This is consistent with comparable gas permeance and experimental OSN results (Fig. 5c). These pore sizes are much smaller than the diameters of the organic solvents used in this work, so in principle no solvent should be able to access them. However, high solvent permeances were observed for PAR membranes with enhanced microporosity, suggesting that the interconnectivity and pore size of PAR networks is enlarged in organic solvents owing to swelling. Simulation and experimental results give relatively higher surface areas and lower densities (Fig. 5d and Supplementary Table 7) for PAR-BHPF and PAR-TTSBI, compared with PAR-DHAQ and PAR-RES networks.

Conclusions

In summary, by using rigid contorted monomers as building blocks for interfacial polymerization, we have demonstrated the formation of ultrathin crosslinked polyarylate nanofilm membranes of enhanced microporosity. These membranes offer outstanding performance in organic solvent nanofiltration, where they are both more permeable and more selective than commercially available and previously reported membranes, showing high solvent permeance over a wide range of solvent polarity. The tunable free volume of polyarylate networks in the solid state was confirmed by gas adsorption and permeation, and molecular simulation. The interfacial polymerization process is used to produce reverse osmosis membranes for desalination that have revolutionized water purification globally. Furthermore, crosslinked polyimide ultrafiltration supports and the monomers used to form the polyarylate nanofilms are both commercially available, making up-scaling feasible. This work might inspire interfacial synthesis of the rapidly growing family of microporous polymers, such as PIMs, MOFs, covalent organic frameworks, and conjugated microporous polymers, to obtain ultrathin microporous nanofilm-based membranes with great potential for applications in molecular separations, including gas separation, organic solvent nanofiltration, water purification and desalination, and hydrocarbon separations in the petrochemical industry.

Methods

Methods and any associated references are available in the online version of the paper.

Received 10 December 2015; accepted 5 April 2016; published online 2 May 2016

References

1. Gin, D. L. & Noble, R. D. Designing the next generation of chemical separation membranes. *Science* **332,** 674–676 (2011).
2. Marchetti, P., Jimenez Solomon, M. F., Szekely, G. & Livingston, A. G. Molecular separation with organic solvent nanofiltration: a critical review. *Chem. Rev.* **114,** 10735–10806 (2014).
3. Guiver, M. D. & Lee, Y. M. Polymer rigidity improves microporous membranes. *Science* **339,** 284–285 (2013).
4. Freeman, B. D. Basis of permeability/selectivity tradeoff relations in polymeric gas separation membranes. *Macromolecules* **32,** 375–380 (1999).
5. Park, H. B. *et al*. Polymers with cavities tuned for fast selective transport of small molecules and ions. *Science* **318,** 254–258 (2007).
6. Du, N. *et al*. Polymer nanosieve membranes for CO_2-capture applications. *Nature Mater.* **10,** 372–375 (2011).
7. Carta, M. *et al*. An efficient polymer molecular sieve for membrane gas separations. *Science* **339,** 303–307 (2013).
8. Song, Q. *et al*. Photo-oxidative enhancement of polymeric molecular sieve membranes. *Nature Commun.* **4,** 1918 (2013).
9. Song, Q. *et al*. Controlled thermal oxidative crosslinking of polymers of intrinsic microporosity towards tunable molecular sieve membranes. *Nature Commun.* **5,** 4813 (2014).
10. Rodenas, T. *et al*. Metal–organic framework nanosheets in polymer composite materials for gas separation. *Nature Mater.* **14,** 48–55 (2014).
11. Karan, S., Jiang, Z. & Livingston, A. G. Sub-10 nm polyamide nanofilms with ultrafast solvent transport for molecular separation. *Science* **348,** 1347–1351 (2015).
12. Karan, S. *et al*. Ultrafast viscous permeation of organic solvents through diamond-like carbon nanosheets. *Science* **335,** 444–447 (2012).
13. Li, H. *et al*. Ultrathin, molecular-sieving graphene oxide membranes for selective hydrogen separation. *Science* **342,** 95–98 (2013).
14. Nair, R. R. *et al*. Unimpeded permeation of water through helium-leak–tight graphene-based membranes. *Science* **335,** 442–444 (2012).
15. Peng, Y. *et al*. Metal-organic framework nanosheets as building blocks for molecular sieving membranes. *Science* **346,** 1356–1359 (2014).
16. Kim, H. W. *et al*. Selective gas transport through few-layered graphene and graphene oxide membranes. *Science* **342,** 91–95 (2013).
17. Yaghi, O. M. *et al*. Reticular synthesis and the design of new materials. *Nature* **423,** 705–714 (2003).
18. Kitagawa, S., Kitaura, R. & Noro, S.-i. Functional porous coordination polymers. *Angew. Chem. Int. Ed.* **43,** 2334–2375 (2004).
19. El-Kaderi, H. M. *et al*. Designed synthesis of 3D covalent organic frameworks. *Science* **316,** 268–272 (2007).
20. Côté, A. P. *et al*. Porous, crystalline, covalent organic frameworks. *Science* **310,** 1166–1170 (2005).
21. Jones, J. T. A. *et al*. Modular and predictable assembly of porous organic molecular crystals. *Nature* **474,** 367–371 (2011).
22. Tozawa, T. *et al*. Porous organic cages. *Nature Mater.* **8,** 973–978 (2009).
23. Song, Q. *et al*. Porous organic cage thin films and molecular-sieving membranes. *Adv. Mater.* **28,** 2629–2637 (2016).

24. Li, Y. S. *et al*. Controllable synthesis of metal-organic frameworks: from MOF nanorods to oriented MOF membranes. *Adv. Mater.* **22,** 3322–3326 (2010).
25. Brown, A. J. *et al*. Interfacial microfluidic processing of metal-organic framework hollow fiber membranes. *Science* **345,** 72–75 (2014).
26. Dobrzańska, L., Lloyd, G. O., Esterhuysen, C. & Barbour, L. J. Guest-induced conformational switching in a single crystal. *Angew. Chem. Int. Ed.* **45,** 5856–5859 (2006).
27. McKeown, N. B. & Budd, P. M. Polymers of intrinsic microporosity (PIMs): organic materials for membrane separations, heterogeneous catalysis and hydrogen storage. *Chem. Soc. Rev.* **35,** 675–683 (2006).
28. McKeown, N. B. *et al*. Polymers of intrinsic microporosity (PIMs): bridging the void between microporous and polymeric materials. *Chem. Eur. J.* **11,** 2610–2620 (2005).
29. Carta, M. *et al*. Triptycene induced enhancement of membrane gas selectivity for microporous Tröger's base polymers. *Adv. Mater.* **26,** 3526–3531 (2014).
30. Ghanem, B. S., Swaidan, R., Litwiller, E. & Pinnau, I. Ultra-microporous triptycene-based polyimide membranes for high-performance gas separation. *Adv. Mater.* **26,** 3688–3692 (2014).
31. McKeown, N. B. & Budd, P. M. Exploitation of intrinsic microporosity in polymer-based materials. *Macromolecules* **43,** 5163–5176 (2010).
32. Budd, P. M. *et al*. Solution-processed, organophilic membrane derived from a polymer of intrinsic microporosity. *Adv. Mater.* **16,** 456–459 (2004).
33. Budd, P. M. *et al*. Gas separation membranes from polymers of intrinsic microporosity. *J. Membr. Sci.* **251,** 263–269 (2005).
34. Fritsch, D. *et al*. High performance organic solvent nanofiltration membranes: development and thorough testing of thin film composite membranes made of polymers of intrinsic microporosity (pims). *J. Membr. Sci.* **401–402,** 222–231 (2012).
35. Tsarkov, S. *et al*. Solvent nanofiltration through high permeability glassy polymers: effect of polymer and solute nature. *J. Membr. Sci.* **423–424,** 65–72 (2012).
36. Gorgojo, P. *et al*. Ultrathin polymer films with intrinsic microporosity: anomalous solvent permeation and high flux membranes. *Adv. Funct. Mater.* **24,** 4729–4737 (2014).
37. Murphy, T. M. *et al*. Physical aging of layered glassy polymer films via gas permeability tracking. *Polymer* **52,** 6117–6125 (2011).
38. Ichinose, I., Kurashima, K. & Kunitake, T. Spontaneous formation of cadmium hydroxide nanostrands in water. *J. Am. Chem. Soc.* **126,** 7162–7163 (2004).
39. Karan, S. *et al*. Ultrathin free-standing membranes from metal hydroxide nanostrands. *J. Membr. Sci.* **448,** 270–291 (2013).
40. Qian, H., Zheng, J. & Zhang, S. Preparation of microporous polyamide networks for carbon dioxide capture and nanofiltration. *Polymer* **54,** 557–564 (2013).
41. Jimenez Solomon, M. F., Bhole, Y. & Livingston, A. G. High flux membranes for organic solvent nanofiltration (OSN)—interfacial polymerization with solvent activation. *J. Membr. Sci.* **423–424,** 371–382 (2012).
42. Ameloot, R. *et al*. Interfacial synthesis of hollow metal–organic framework capsules demonstrating selective permeability. *Nature Chem.* **3,** 382–387 (2011).
43. Chung, J. Y., Lee, J.-H., Beers, K. L. & Stafford, C. M. Stiffness, strength, and ductility of nanoscale thin films and membranes: a combined wrinkling–cracking methodology. *Nano Lett.* **11,** 3361–3365 (2011).
44. Weber, J., Su, Q., Antonietti, M. & Thomas, A. Exploring polymers of intrinsic microporosity—microporous, soluble polyamide and polyimide. *Macromol. Rapid Commun.* **28,** 1871–1876 (2007).
45. Robeson, L. M. The upper bound revisited. *J. Membr. Sci.* **320,** 390–400 (2008).
46. Du, N., Park, H. B., Dal-Cin, M. M. & Guiver, M. D. Advances in high permeability polymeric membrane materials for CO_2 separations. *Energy Environ. Sci.* **5,** 7306–7322 (2012).
47. Abbott, L. & Colina, C. *Polymatic: A Simulated Polymerization Algorithm* (2013); https://nanohub.org/resources/17278

Acknowledgements

This work was financially supported by the Engineering and Physical Sciences Research Council (EPSRC, UK), 7th Framework Programme of the European Commission's Marie Curie Initiative, NEMOPUR Project (M.F.J.-S.), Imperial College Junior Research Fellowship (Q.S.), and Royal Society University Research Fellowship (K.E.J.). The authors are grateful to P. R. J. Gaffney for assisting with monophasic reactions.

Author contributions

M.F.J.-S. and A.G.L. conceived the idea. M.F.J.-S., Q.S. and A.G.L. designed the research. M.F.J.-S. and Q.S. performed experiments, including synthesis of materials and membranes, and characterization analyses. M.F.J.-S. carried out organic solvent nanofiltration. Q.S. performed gas permeation measurements. K.E.J. performed molecular simulations. M.M.-I. assisted with synthesis of PAR/PI nanofilm composite membranes. M.F.J.-S., Q.S. and A.G.L. wrote the manuscript. A.G.L. guided the project. All of the authors participated in the discussion and read the manuscript.

Additional information

Supplementary information is available in the online version of the paper. Reprints and permissions information is available online at www.nature.com/reprints. Correspondence and requests for materials should be addressed to A.G.L.

Competing financial interests

The authors declare no competing financial interests.

Methods

Synthesis of polymers. Polyarylate solids were prepared by interfacial polymerization or through monophasic reactions. Four different phenol monomers were used: contorted monomers including 5,5′,6,6′-tetrahydroxy-3,3,3′,3′-tetramethylspirobisindane (TTSBI, Alfa Aesar) and 9,9-bis(4-hydroxyphenyl) fluorene (BHPF, Sigma-Aldrich), and planar monomers including 2,6-dihydroxyanthraquinone (DHAQ, Sigma-Aldrich), and 1,3-benzenediol (resorcinol, RES, Sigma-Aldrich). For interfacial polymerization, each phenol monomer was dissolved in a diluted sodium hydroxide aqueous solution (pH 13) with a molar ratio of 4:1 (NaOH to TTSBI and BHPF), and 2:1 (NaOH to DHAQ and RES) (throughout this study), with concentrations of TTSBI (1 wt%), BHPF (1 wt%), DHAQ (2 wt%), and RES (2 wt%). The sodium phenoxides were then reacted interfacially with trimesoyl chloride (TMC, Sigma-Aldrich) dissolved in hexane (0.2 wt % by volume) under rigorous stirring for 2 min. The resulting polymers were then washed thoroughly with water, followed by hexane. They were then freeze-dried from hexane and dried at 120 °C under vacuum for 12 h. For monophasic polymerization reactions, 1 g phenol was mixed with TMC at 1:1 molar ratio dissolved in dry degassed THF (40–60 ml). An 11-fold molar excess of dry pyridine was added through a syringe under nitrogen gas and stirring. After reflux for 20 h, a precipitate was formed, which was washed with 1 M HCl solution, water and THF. It was subsequently dried through freeze drying, and then at 120 °C in a vacuum oven for 12 h.

Synthesis of freestanding polymer nanofilms. Freestanding PAR nanofilms were fabricated by interfacial polymerization. Phenol monomers were dissolved in aqueous basic NaOH solutions with varied concentrations of TTSBI (1 wt%), BHPF (1 wt%) and RES (2 wt%). A solution of 0.1% (w/v) TMC in hexane was slowly added to the aqueous solution, and allowed to react for 2 min. Afterwards, the resulting nanofilms were immediately withdrawn from the interface with a clean glass substrate, washed in clean distilled water, and transferred to an anodized aluminium oxide membrane disc (Anodisc, Whatman) with a surface layer of 20 nm nanopores. To form a thicker nanofilm (200 nm) for solvent permeation studies, a 1% (w/v) TMC in hexane solution was used and reacted with an aqueous solution of BHPF (1 wt%) in NaOH for 2 min.

Fabrication of ultrafiltration support membranes. Crosslinked polyimide (PI) ultrafiltration support membranes were prepared and conditioned following the same methodology as previously reported by our group[48]. In brief, a polymer dope solution was prepared by dissolving 22% (w/w) polyimide (P84) (HP Polymer GmbH) in dimethylsulphoxide and stirring overnight until complete dissolution. A viscous solution (2,250 cP at 22 °C) was formed, and allowed to stand for 10 h to remove air bubbles. The dope solution was then cast on the smooth side of a polypropylene non-woven backing (Novatexx 2471) at a casting speed of 0.035 m s^{-1} using a Sepratek continuous casting machine with a casting knife set at a gap of 250 μm located in a room held at constant temperature (21 °C). Immediately after casting, the membrane was immersed in a deionized water bath at 21 °C where phase inversion occurred. After 15 min, membranes were transferred to a fresh water bath and left for an hour. The wet membranes were then immersed in an isopropanol exchange bath to remove any residual water and preparation solvents. The support membranes were crosslinked as described elsewhere[48], by immersing the membrane in a solution of 1,6-hexanediamine (Sigma-Aldrich) in isopropanol (120 g l^{-1}) for 16 h at room temperature. The membranes were then removed from the crosslinking bath and washed with isopropanol for 3 h to remove any residual 1,6-hexanediamine. The support membranes were conditioned with polyethylene glycol 400 (VWR) before the interfacial polymerization reaction. The conditioning step involved immersing the membrane overnight in a conditioning agent bath comprising polyethylene glycol 400 in isopropanol at a volume ratio of 3:2. The membranes were then dried at room temperature inside a fume hood.

Nanofilm composite membranes. Nanofilm composite membranes for OSN were prepared by interfacial polymerization directly on conditioned crosslinked polyimide (PI) P84 ultrafiltration supports using different monomers (see Supplementary Fig. 2). Interfacial polymerization to form polyarylate nanofilms was performed by exposing the surface of the ultrafiltration support to an aqueous basic solution of sodium phenoxide, including TTSBI (1 wt%), BHPF (1 wt%), DHAQ (2 wt%) and RES (2 wt%) for 2 min. The phenoxide-loaded support membranes were then pressed with a roller and air was applied to remove excess solution. The membranes were then exposed to TMC in hexane (0.1 % w/v) for 2 min. The resulting membranes were withdrawn from the hexane solution, dried in air, and cured in a ventilated oven at 85 °C for 10 min to complete crosslinking. The membranes were then stored in distilled water at 4 °C. As a control, a conditioned polyimide ultrafiltration support was immersed in the aqueous and organic phases without monomers and cured in a ventilated oven under the same conditions (see Supplementary Fig. 14).

Nanofilm composite membranes for gas permeation tests were prepared by *in situ* polymerization of polyarylate nanofilms. First, a thin layer (about 50 nm) of poly(trimethylsilyl)propyne (PTMSP, Fluorochem) was coated on the anodized aluminium oxide support (diameter of 25 mm) by spin-coating a PTMSP solution in chloroform (0.5 wt%) at 2,000 r.p.m. for 1 min. Then a drop of solution of TMC (1 wt%) in hexane was spin-coated on the alumina-PTMSP substrates at 2,000 r.p.m. for 1 min. Subsequently, a drop of phenoxide solution (1 wt%) in water was added to the surface and spin-coated at 2,000 r.p.m. for 1 min. *In situ* polymerization occurs at the interface forming a thin polyarylate nanofilm.

Characterization methods. Fourier transform infrared spectra were recorded on a Perkin-Elmer Spectrometer 100, with samples mounted on a zinc-selenium/diamond plate. Thermal analyses were performed with a thermogravimetric analyser (TGA) Q500 (TA Instruments). Polymer powders were heated from room temperature to 900 °C at 10 °C min^{-1} in N_2. Densities of polymer solids were measured using a Micrometrics Accupyc 1340 helium pycnometer equipped with a 5 cm^3 insert. The obtained values are the mean and standard deviation from a cycle of 10 measurements. Samples were evacuated thoroughly under vacuum at 120 °C for 24 h before measurements. Low-pressure gas sorption was performed using a Micrometrics TriStar or ASAP2050 surface area analyser. Samples were dried at 120 °C under vacuum for 12 h, and then loaded into the apparatus and degassed at 120 °C for 12 h. Nitrogen adsorption isotherms were measured at 77 K and CO_2 sorption isotherms were measured at 273 K. Wide-angle X-ray scattering was performed with a Bruker D8 machine operated at 40 mA and 40 kV using Cu Kα radiation with a step of 0.02° per second. SEM was carried out using a field-emission gun scanning electron microscope (LEO 1525 from Karl Zeiss) or a Hitachi S5500 microscope. For cross-sectional SEM imaging, the polymer films were freeze-fractured in liquid nitrogen. Samples were sputter-coated with a thin layer of chromium or gold and palladium. AFM imaging was performed on a Veeco AFM Dimension 3100 equipped with a DAFMLN Dimension AFM scan head and a Nanoscope VI controller. Samples were attached to glass slides using a double-sided tape. The scans were performed in an air medium. The images were scanned in tapping mode using silicone cantilevers having a nominal diameter of less than 10 nm. Scanning was performed at a speed of 1.3 Hz, and a scan size of 5 μm was used for standard images. Bruker 'NanoScope Analysis beta' or 'Gwyddion 2.38 SPM data visualization and analysis software' were used to process the AFM images. Roughness was estimated from at least three images of the same membrane scanned over an area of 5 μm × 5 μm from each sample. To measure the thickness from AFM, polyarylate-TTSBI nanofilms were made on non-crosslinked PI support, so that the support could be dissolved and the nanofilm analysed on its own. Nanofilm composite membranes were transferred in a flipped configuration onto a silicon wafer and the polyimide support was dissolved. A scratch was made to expose the wafer surface. The thickness of the nanofilm was estimated from the height difference between the silicon and the upper surface of the nanofilm using a one-dimensional statistical function. The mechanical properties of polyarylate nanofilms were measured using a wrinkle-based method[11,43,49], by generating compressive stress in the nanofilms supported on stretched poly(dimethylsiloxane) strips (details are given in Supplementary Fig. 13). The Young's modulus are derived and presented in Supplementary Table 1.

Organic solvent nanofiltration. Nanofiltration performance was evaluated in terms of permeance of organic solvent and rejection of oligomers or dye molecules with varied molecular weights. Most nanofiltration experiments were carried out in repeats of three in a crossflow system at 30 °C and 30 bar. The rejection of Rose Bengal in isopropanol was conducted in repeats of three in a dead-end stirred cell (500 r.p.m.) at 30 °C and 30 bar. The nanofiltration through a thick freestanding PAR-BHPF nanofilm supported on alumina was carried out in a dead-end stirred cell (500 r.p.m.) at 30 °C and 10 bar. The crossflow filtration system consisted of two sets of four cells in series connected in parallel. The effective membrane area in each cell was 14 cm^2, membrane discs were placed into eight crossflow cells connected in series, and with a feed flow of 100 l h^{-1}. Permeate samples for flux measurements were collected at intervals of 1 h, and samples for rejection evaluations were taken after 24 h, when steady permeate flux was achieved. Before solute rejection tests, the selected pure solvent was filtered through the membrane for 1 h to remove impurities, including polyethylene glycol 400. The solute rejection test was carried out using two standard solutions. The first was a standard feed solution comprised of a homologous series of polystyrene oligomers (PS) dissolved in solvent. The solvents used were methanol, acetone, THF and toluene. The styrene oligomer mixture contained 2 g l^{-1} each of PS 580 and PS 1090 (Agilent Technologies), and 0.01 g l^{-1} of α-methylstyrene dimer (Sigma-Aldrich)[50]. Analysis of the styrene oligomers was undertaken using an Agilent HPLC system with an ultraviolet–visible detector set at a wavelength of 264 nm. Separation was achieved using a reverse-phase column (C18-300, 250 × 4.6 mm). The mobile phase consisted of 35 vol% analytical-grade water and 65 vol% tetrahydrofuran with 0.1 vol% trifluoroacetic acid. The second set of standard markers solution consisted of a solution containing one of the following dyes (Sigma-Aldrich) in methanol: brilliant blue (826 g mol^{-1}); crystal violet (408 g mol^{-1}); disperse red 1

(314 g mol^{-1}); and chrysoidine G (249 g mol^{-1}), or Rose Bengal (1,017 g mol^{-1}) in isopropanol (see Supplementary Table 4). Analysis of the dyes was carried out using ultraviolet–visible. Solvent permeance (J, l m^{-2} h^{-1} bar^{-1}) was determined by measuring permeate volume (V) per unit area (A) per unit time (t) per applied pressure (p) according to the following equation: $J = V/(A \times t \times p)$. The rejection ($R_i$) of markers was calculated from $R_i = (1 - (C_{P,i}/C_{F,i})) \times 100\%$, where $C_{P,i}$ and $C_{F,i}$ correspond to marker concentrations in the permeate and the feed, respectively.

Gas permeation. Single-gas transport properties were measured using a time-lag apparatus described in detail elsewhere[9,51]. The gas permeation tests were carried out at a temperature of 22 °C and feed pressure of 1 bar with He, H_2, CO_2, O_2, N_2 and CH_4 (research grade, BOC, UK). Each membrane was thoroughly evacuated with a vacuum pump before measurements. The gas permeance (J, GPU, 1 GPU = 10^{-6} cm^3 (STP) cm^{-2} s^{-1} cm Hg^{-1}) was derived from the volume of gas flowing across the membrane per unit of pressure difference. The ideal selectivity for a gas pair (A/B) is calculated from the ratio of their permeances. The uncertainties of gas permeances are within ±10%, and selectivity within ±15%. Intrinsic gas permeability (P) was calculated by multiplying the permeance by the thickness of the selective polyarylate layer ($P = J \times L$). P is expressed in barrer (1 barrer = 10^{-10} cm^3 (STP) cm cm^{-2} s^{-1} cm Hg^{-1}).

Molecular simulation. For the generation of amorphous polymer models, we used the simulated polymerization algorithm Polymatic[47,52]. Polymatic was originally developed for amorphous network polymers, including PIM-1[52], sulfonated PIMs[53], crosslinked polymers[54], and conjugated microporous polymers[55]. We generated five models for each of the four polyarylate polymer models, PAR-BHPF, PAR-TTSBI, PAR-DHAQ and PAR-RES. All structures were described using the polymer-consistent force field[56]. Partial charges were calculated for the repeat units by fitting atomic charges from the output of Gaussian09[57] calculations at the HF/6-31G* level of theory. The chlorides from the acyl chlorides and the hydrogens of the —OH group of the alcohols were removed in the input molecular fragments, as these are not present in the final structure. Initially we loaded periodic cubic cells, of cell dimensions of 70 Å, at low densities of 0.4 g cm^{-3} and a ratio of two acyl chloride molecules to three phenol molecules. Polymerization steps were then sequentially performed between reactive atoms on opposite monomers within a cutoff of 6 Å with intermediate molecular dynamics steps to allow the structure to adapt. The reactive end groups were the carbons of the carbonyls on the TMC and the oxygens of the alcohol molecules. The final polymerized structures were then annealed through a 21-step molecular dynamics equilibration, with the protocol as detailed elsewhere[52]. The LAMMPS package (http://lammps.sandia.gov)[58] was used throughout, both for the polymerization algorithm and the 21-step relaxation procedure[52]. For any unreacted end groups after polymerization, we terminated them appropriately, with carboxylic acid end groups for TMC and —OH end groups for the alcohol. We used carboxylic acids for the TMC as following the polymers being exposed to water in air, all chlorides in the group would undergo hydrolysis by nucleophilic addition/elimination to form carboxylic acids. We generated five models for each system to ensure adequate sampling and averaged the properties across them. For void analysis, Zeo++[59,60] was employed. This calculates void space, the largest cavity diameter, pore limiting diameter, pore size distribution and through a Voronoi decomposition the interconnectivity of void space. The surface area accessible to N_2 was calculated with a probe radius of 1.55 Å, equivalent to the van der Waals radius of N_2. The atomic radii for the host and for N_2 were taken from the Cambridge Crystallographic Database Centre guidelines (http://www.ccdc.cam.ac.uk/products/csd/radii).

References

48. See Toh, Y. H., Lim, F. W. & Livingston, A. G. Polymeric membranes for nanofiltration in polar aprotic solvents. *J. Membr. Sci.* **301,** 3–10 (2007).
49. Stafford, C. M. *et al*. A buckling-based metrology for measuring the elastic moduli of polymeric thin films. *Nature Mater.* **3,** 545–550 (2004).
50. See Toh, Y. H. *et al*. In search of a standard method for the characterisation of organic solvent nanofiltration membranes. *J. Membr. Sci.* **291,** 120–125 (2007).
51. Song, Q. *et al*. Zeolitic imidazolate framework (ZIF-8) based polymer nanocomposite membranes for gas separation. *Energy Environ. Sci.* **5,** 8359–8369 (2012).
52. Abbott, L., Hart, K. & Colina, C. Polymatic: a generalized simulated polymerization algorithm for amorphous polymers. *Theor. Chem. Acc.* **132,** 1–19 (2013).
53. Hart, K. E., Abbott, L. J., McKeown, N. B. & Colina, C. M. Toward effective CO_2/CH_4 separations by sulfur-containing pims via predictive molecular simulations. *Macromolecules* **46,** 5371–5380 (2013).
54. Abbott, L. J., Hughes, J. E. & Colina, C. M. Virtual synthesis of thermally cross-linked copolymers from a novel implementation of polymatic. *J. Phys. Chem. B* **118,** 1916–1924 (2014).
55. Abbott, L. J. & Colina, C. M. Porosity and ring formation in conjugated microporous polymers. *J. Chem. Eng. Data* **59,** 3177–3182 (2014).
56. Sun, H. Force field for computation of conformational energies, structures, and vibrational frequencies of aromatic polyesters. *J. Comput. Chem.* **15,** 752–768 (1994).
57. Frisch, M. J. *et al*. *Gaussian 09. Revision A.02* (Gaussian, 2009).
58. Plimpton, S. Fast parallel algorithms for short-range molecular dynamics. *J. Comput. Phys.* **117,** 1–19 (1995).
59. Willems, T. F. *et al*. Algorithms and tools for high-throughput geometry-based analysis of crystalline porous materials. *Micropor. Mesopor. Mater.* **149,** 134–141 (2012).
60. Pinheiro, M., Martin, R. L., Rycroft, C. H. & Haranczyk, M. High accuracy geometric analysis of crystalline porous materials. *CrystEngComm* **15,** 7531–7538 (2013).